



HAL
open science

Ultrahigh-current-density niobium disulfide catalysts for hydrogen evolution

Jieun Yang, Abdul Rahman Mohmad, Yan Wang, Raymond Fullon, Xiuju Song, Fang Zhao, Ibrahim Bozkurt, Mathias Augustin, Elton Santos, Hyeon Suk Shin, et al.

► **To cite this version:**

Jieun Yang, Abdul Rahman Mohmad, Yan Wang, Raymond Fullon, Xiuju Song, et al.. Ultrahigh-current-density niobium disulfide catalysts for hydrogen evolution. *Nature Materials*, 2019, 18 (12), pp.1309-1314. 10.1038/s41563-019-0463-8. hal-02394953

HAL Id: hal-02394953

<https://hal.umontpellier.fr/hal-02394953v1>

Submitted on 24 Oct 2023

HAL is a multi-disciplinary open access archive for the deposit and dissemination of scientific research documents, whether they are published or not. The documents may come from teaching and research institutions in France or abroad, or from public or private research centers.

L'archive ouverte pluridisciplinaire **HAL**, est destinée au dépôt et à la diffusion de documents scientifiques de niveau recherche, publiés ou non, émanant des établissements d'enseignement et de recherche français ou étrangers, des laboratoires publics ou privés.



**QUEEN'S
UNIVERSITY
BELFAST**

Ultrahigh-current-density niobium disulfide catalysts for hydrogen evolution

Yang, J., Mohmad, A. R., Wang, Y., Fullon, R., Song, X., Zhao, F., Bozkurt, I., Augustin, M., Santos, E. J. G., Shin, H. S., Zhang, W., Voiry, D., Jeong, H. Y., & Chhowalla, M. (2019). Ultrahigh-current-density niobium disulfide catalysts for hydrogen evolution. *Nature Materials*, 18(2019), 1309. <https://doi.org/10.1038/s41563-019-0463-8>

Published in:
Nature Materials

Document Version:
Peer reviewed version

Queen's University Belfast - Research Portal:
[Link to publication record in Queen's University Belfast Research Portal](#)

Publisher rights
Copyright 2019 Nature Research. This work is made available online in accordance with the publisher's policies. Please refer to any applicable terms of use of the publisher.

General rights
Copyright for the publications made accessible via the Queen's University Belfast Research Portal is retained by the author(s) and / or other copyright owners and it is a condition of accessing these publications that users recognise and abide by the legal requirements associated with these rights.

Take down policy
The Research Portal is Queen's institutional repository that provides access to Queen's research output. Every effort has been made to ensure that content in the Research Portal does not infringe any person's rights, or applicable UK laws. If you discover content in the Research Portal that you believe breaches copyright or violates any law, please contact openaccess@qub.ac.uk.

Open Access
This research has been made openly available by Queen's academics and its Open Research team. We would love to hear how access to this research benefits you. – Share your feedback with us: <http://go.qub.ac.uk/oa-feedback>

1 **Ultrahigh current density niobium disulfide catalysts for hydrogen evolution**

2 Jieun Yang^{1,†}, Abdul Rahman Mohmad^{2,†}, Yan Wang¹, Raymond Fullon¹, Xiuju Song^{1,3}, Fang
3 Zhao⁴, Ibrahim Bozkurt¹, Mathias Augustin⁵, Elton J. G. Santos^{5*}, Hyeon Suk Shin⁶, Damien
4 Voiry⁷, Hu Young Jeong^{8,*}, Manish Chhowalla^{1,3*#}

5 **Affiliations:**

6 ¹*Materials Science and Engineering, Rutgers University, 607 Taylor Road, Piscataway, New*
7 *Jersey 08854, USA.*

8 [#]*Current Address: Department of Materials Science & Metallurgy, University of Cambridge, 27*
9 *Charles Babbage Road, Cambridge CB3 0FS, UK.*

10 ²*Institute of Microengineering and Nanoelectronics, National University of Malaysia (UKM),*
11 *43600 Bangi, Selangor, Malaysia*

12 ³*SZU-RUT Collaborative Innovation Center for Optoelectronic Science & Technology,*
13 *International Collaborative Laboratory of 2D Materials for Optoelectronics Science and*
14 *Technology of Ministry of Education, College of Optoelectronic Engineering, Shenzhen*
15 *University, Shenzhen 518060, China.*

16 ⁴*Department of Physics, Princeton University, Jadwin Hall, Princeton New Jersey 08544, USA*

17 ⁵*School of Mathematics and Physics, Queen's University Belfast, BT71NN, United Kingdom*

18 ⁶*Department of Chemistry and Department of Energy Engineering, Low-Dimensional Carbon*
19 *Materials Center, Ulsan National Institute of Science and Technology (UNIST), UNIST-gil 50,*
20 *Ulsan 44919, Republic of Korea*

21 ⁷*Institut Européen des Membranes (I.E.M.), University of Montpellier, Place Eugène Bataillon,*
22 *34095 Montpellier, France*

23 ⁸*UNIST Central Research Facilities (UCRF) and School of Materials Science and Engineering,*
24 *UNIST, Ulsan 689-798, Republic of Korea*

25 *Correspondence to: e.santos@qub.ac.uk, hulex@unist.ac.kr and mc209@cam.ac.uk

26 [†] *These authors contributed equally to this work.*

27
28
29
30
31
32
33
34
35

36
37 **Two-dimensional metallic transition metal dichalcogenides (2D TMDs) such as 1T phases**
38 **of MoS₂^{1,2} and WS₂³, NbS₂⁴, TaS₂⁴⁻⁶ and VS₂^{7,8} have been studied as potentially**
39 **inexpensive and earth abundant electrocatalysts for the hydrogen evolution reaction**
40 **(HER). The performance of HER catalysts is typically evaluated in terms of overpotential**
41 **at which the reaction starts and the Tafel slope – a measure of the over-potential required**
42 **to increase a reaction by a factor of 10. The overpotential and Tafel slope values of metallic**
43 **phases and edges⁹ of 2D TMDs approach those of Pt nanoparticles – the best HER catalyst.**
44 **However, despite substantial progress the overall current density of 2D TMD catalysts**
45 **remains orders of magnitude lower (~ 10 – 100 mA-cm⁻²) than industrial Pt and Ir**
46 **electrolyzers (> 1,000 mA-cm⁻²)^{10,11}. Here, we report the synthesis of three dimensional**
47 **(3D) niobium disulfide (Nb_{1+x}S₂ where *x* is ~ 0.35)¹² as a HER catalyst that is capable of**
48 **evolving hydrogen at current densities of > 5,000 mA-cm⁻² at an overpotential of ~420 mV**
49 ***versus* reversible hydrogen electrode (RHE). We find the exchange current density at 0 V**
50 **for 2H phase Nb_{1.35}S₂ catalysts to be ~ 0.8 mA-cm⁻² (comparable to that of noble metals),**
51 **corresponding to a turnover frequency of ~ 0.2 s⁻¹. We demonstrate a proof of concept**
52 **electrolyzer based on 2H Nb_{1.35}S₂ cathode that is capable of generating current densities of**
53 **1000 mA-cm⁻². Our theoretical results reveal that the Nb_{1.35}S₂ with Nb terminated surface**
54 **has free energy for hydrogen adsorption that is close to thermoneutral, facilitating HER.**
55 **The Nb_{1+x}S₂ could therefore be a viable non-precious metal catalyst for practical**
56 **electrolyzers used to generate hydrogen.**

57
58 Ultra-thin layers of TMD catalysts exhibit improved electrocatalytic performance due to efficient
59 charge injection and transfer to active sites^{13,14}. Increasing the conductivity via engineering of
60 metallic phases^{2,15,16} and edges^{14,17-19} also leads to substantial improvement in catalytic
61 properties. To this end, metallic 1T phase of semiconducting MoS₂ induced by lithium
62 chemistry^{1,2,20} has been widely studied for HER catalysis. Recently, multi-layers of thin metallic
63 TMDs such as NbS₂⁴, TaS₂⁵, and VS₂⁷ have also been studied for HER. The key advantage of
64 metallic TMDs according to theory is that the entire basal plane is catalytically active for the
65 HER^{4,21,22}, unlike in semiconducting MoS₂ where only the metallic edges are active⁹. However,
66 in contrast with noble metal catalysts such as Pt nanoparticles, the electronic structure of

67 atomically thin materials is strongly influenced by local electrochemical reactions. For example,
68 in the case of metallic 1T phase MoS₂, the adsorption of protons on the surface – the first step in
69 the HER – can dramatically reduce the conductivity of the 2D nanosheets²¹, which can slow
70 down the reaction kinetics and reduce the overall current density. Thus, a fine balance must be
71 achieved between reducing the thickness of catalysts and maintaining metallic nature of 2D
72 materials to maximize catalytic performance.

73
74 NbS₂ is a layered material that can exist in the hexagonal (2H phase) or rhombohedral (3R)
75 crystal configurations (see Extended Data Fig. 1a,b,d,e). Metallic 2H phase NbS₂ has been
76 predicted to be one of the most efficient electrocatalysts for the HER among the different types
77 of TMDs²². In addition to the 2H and 3R phases, an unexplored non-layered 3D polytype with
78 Nb_{1+x}S₂ (where x is ~ 0.35) stoichiometry, first synthesized in 1960 (Ref¹²), consisting of excess
79 niobium strongly bonded to NbS₂ layers is also stable (see Extended Data Fig. 1c,f). We find that
80 the exceed Nb Nb_{1+x}S₂ phase can be synthesized by adjusting the CVD growth parameters (see
81 Methods). Atomic force microscopy (AFM) image of typical Nb_{1+x}S₂ crystals synthesized by
82 chemical vapor deposition is shown in Figure 1a. Films of varying thicknesses ranging from 2
83 nm to 50 nm with lateral dimensions of $\sim 0.5 - 1 \mu\text{m}$ were realized by CVD on substrates such as
84 SiO₂ and glassy carbon. We find that the phase of NbS₂ is dependent on the thickness of the
85 material (Extended Data Fig. 2a-c). The electron diffraction patterns corresponding to the phases
86 as a function of thickness are provided in Extended Data Fig. 2d,e. In particular, 2H – Nb_{1+x}S₂ is
87 predominantly observed in crystals with thickness of less than ~ 20 nm while the 3R phase is
88 primarily stable for thicker samples. High-resolution annular dark field (ADF) cross-sectional
89 STEM images of Nb_{1+x}S₂ clearly reveal Nb in both 2H phase (Figure 1b) and the 3R phase
90 (Figure 1c). The $d_{(0002)}$ spacing for the 2H excess Nb phase (6.35 \AA , $c = 12.60 \text{ \AA}$) was found to
91 be close to the theoretical value of the Nb_{1.35}S₂ composition. The lower contrast in ADF image of
92 the intercalated Nb planes is attributed to partial occupation of these sites (occupancy of 0.35 in
93 excess layers versus 1 in the NbS₂ 2H and 3R layers). Additional evidence for intercalated Nb
94 atoms in the form of Z contrast scans of atoms and chemical analyses are provided in Extended
95 Data Fig. 3a,b. X-ray diffraction (XRD) spectrum shown in Extended Data Fig. 3c provides
96 additional evidence for the intercalated hexagonal phase of NbS₂. Direct synthesis of intercalated
97 layered compounds with CVD is highly beneficial for preserving the high quality of the material.

98 That is, intercalation involving wet chemistry can lead to undesirable local reactions and
99 deterioration of the material properties.

100
101 The catalytic properties of NbS₂ and other metallic TMDs such as TaS₂ and VS₂ have been
102 measured in several studies^{4,5,7}. The results generally reveal Tafel slopes of ~ 40 mV-dec⁻¹ and
103 low overpotential values of tens of millivolts *vs* RHE. For comparison, the overpotential at which
104 HER proceeds for Pt nanoparticles is 0 V *vs* RHE with a corresponding Tafel slope of ~ 30 mV-
105 dec⁻¹. Despite the promising overpotentials and Tafel slopes achieved with metallic TMD
106 catalysts, the maximum reported current density value has remained around ~ 100 mA-cm⁻². The
107 current density is limited by the multiple layers of metallic TMDs. That is, in contrast to phase
108 transformed 1T metallic MoS₂ nanosheets that are single layered, it is generally challenging to
109 synthesize or exfoliate metal TMDs down to the monolayer. Thus, most metallic NbS₂ and TaS₂
110 catalysts are multilayered and therefore electrons injected from the glassy carbon support must
111 overcome the van der Waals gaps between the layers to reach the active sites on the surface. This
112 increases the charge transfer resistance and thus the catalytic activity has been demonstrated to
113 be inversely related to the number of layers in TMDs²³. In the case of single layers, while the
114 charge transfer kinetics are improved, the current carrying capability is lower and therefore the
115 overall current density that can be achieved is also lower. Furthermore, the recombination of
116 protons with free electrons on the surface of the single layer catalysts (the first step of the
117 reaction) decreases the concentration of free carriers and therefore the conductivity²¹, reducing
118 the kinetics of the HER and lowering the current density.

119
120 We have tested the catalytic performance of metallic 2H Nb_{1.35}S₂ with improved conductivity via
121 elimination of van der Waals gaps between layers. This Nb_{1.35}S₂ phase for HER was directly
122 grown at 1273 K (CVD parameters are described in Methods) on high-quality glassy carbon
123 electrodes. The HER was measured in 0.5M H₂SO₄ electrolyte (see Methods for detailed
124 description of measurements). The current density as a function of potential (*vs* RHE) from 2H,
125 3R NbS₂, and excess Nb 2H phase Nb_{1.35}S₂ along with those from 3R Nb_{1.35}S₂, 2H and 1T
126 phases of MoS₂ and WS₂ ref³, 2H and 3R NbS₂, and Pt for comparison are shown in Figure 2a.
127 It can be clearly seen from the polarization curves that the current density for the 2H Nb_{1.35}S₂ is
128 exceptionally large, reaching 1000 mA-cm⁻² at ~ 370 mV and 5,000 mA-cm⁻² at ~ 420 mV. This

129 current density is obtained from careful analyses of the catalytic active area. We have examined
130 of numerous scanning electron microscope images to determine the areal coverage of catalyst
131 material on the glassy carbon surface. We found that $20\% \pm 5\%$ of the electrode surface is
132 covered by the catalyst particles, see Extended Data Fig. 4. In addition to the areal coverage, we
133 also carefully measured the electrochemical surface area (see Extended Data Fig. 5) to find the
134 roughness factor ($RF = 11 \pm 3$). Using this value, we were able to accurately determine the active
135 area of the catalyst and use it to calculate the current density. To complement the current density
136 measurements, we measured the actual amount of evolved hydrogen using a gas chromatograph
137 (GC, Agilent 7890 B) equipped with molecular sieve 5 \AA capillary column and a thermal
138 conductivity detector (TCD). The measurements were performed in a gas-tight 3-electrode cell.
139 Ar gas was purged in the cell to remove air. The TCD cell was calibrated using known hydrogen
140 amounts (5% and 10 % H_2 balance Ar certified standard gas). The volume of hydrogen evolved
141 by the $2\text{H-Nb}_{1.35}\text{S}_2$ electrodes was measured at two overpotentials. We found that $2\text{H-Nb}_{1.35}\text{S}_2$
142 can evolve H_2 up to $150 \mu\text{mol}\cdot\text{h}^{-1}$ and $300 \mu\text{mol}\cdot\text{h}^{-1}$ at 300mV and 400 mV, respectively. When
143 normalizing the performance to the surface area, the rate of H_2 evolution reaches $\sim 30 \text{ L}\cdot\text{cm}^{-2}\cdot\text{h}^{-1}$
144 equivalent to $6 \text{ mmol}\cdot\text{h}^{-1}\cdot\text{cm}^{-2}$ at 400 mV. the Faradaic efficiency for the HER is typically 100%
145 and therefore the current density is a direct indication of the amount of hydrogen evolved. Thus,
146 careful measurement of the electrochemical surface area to obtain current density is a good
147 indicator of catalyst performance. To confirm this, we measured the Faradaic efficiency using,
148 $FE = \frac{2nF}{Q}$ where n is the moles of hydrogen measured from GC, F is the Faraday constant, Q is
149 the charge obtained from measurements in Figure 2a of the MS ($Q = I \times t$, where I is the current
150 and t is the time). The obtained efficiencies are 96% and 100% at 300 mV and 400 mV,
151 respectively. Thus, the GC measurements confirm the electrochemical measurements and
152 provide additional evidence for the high performance of $2\text{H-Nb}_{1.35}\text{S}_2$.

153
154 It can be seen from Figure 2b, which provides an expanded view of the low overpotential region
155 in Figure 2a, that the cathodic potential at which the HER starts is less than 100 mV
156 (overpotential of $< 150 \text{ mV}$) for the $2\text{H Nb}_{1.35}\text{S}_2$ catalysts. The reaction for metallic $2\text{H Nb}_{1.35}\text{S}_2$
157 phase starts immediately upon application of the potential and proceeds slowly initially but as the
158 potential is increased, it proceeds rapidly with very high current densities. The Tafel slopes
159 shown in Figure 2c provide additional information about the rate limiting step in the catalytic

160 performance. Tafel slope values can vary from 30 mV-dec⁻¹ for Pt –indicating that HER is
161 limited by the recombination of adsorbed hydrogens – to > 120 mV-dec⁻¹ where adsorption of
162 protons limits the catalytic activity. It can be seen that the Tafel slope for 2H phase Nb_{1.35}S₂
163 catalysts is 43 mV-dec⁻¹ (and ~ 38 mV-dec⁻¹ after *iR* correction) at low overpotentials (100 – 120
164 mV), which is comparable to what has been measured for metallic 1T phase MoS₂ and NbS₂ and
165 suggests that the rate limiting reaction is the desorption of hydrogens. At higher potentials (120 –
166 250 mV), the Tafel slope increases to ~ 70 mV-dec⁻¹ (or 65 mV-dec⁻¹ after *iR* correction),
167 suggesting that hydrogen adsorption or diffusion of protons to active sites limits the reaction. To
168 differentiate between these two mechanisms, we made HER measurements under agitation to
169 increase diffusion of protons and found that the results are largely unchanged. These
170 observations are consistent with theoretical results that show that, unlike Pt, metallic TMD
171 catalysts such as NbS₂ possess dilute adsorption of hydrogens on the surface at low potentials but
172 the high activity per site is retained at higher potentials where coverage of adsorbed hydrogens
173 increases ⁴. In addition to the overpotential and Tafel slope, we have also measured the number
174 of hydrogen molecules evolved per second (the turnover frequency, TOF) for the catalysts. We
175 have found that the TOF for the 2H phase Nb_{1.35}S₂ catalysts to be in excess of 100 s⁻¹ at 280 mV.
176 The TOF from this work compares favorably with other reports, as summarized in Figure 2d.
177 The exchange current density at 0 V for the Nb_{1.35}S₂ phase catalysts was found to be ~ 0.8 mA-
178 cm⁻² which corresponds to a TOF of 0.17 s⁻¹. For comparison, the exchange current density for Pt
179 (111) is 0.5 – 1 mA-cm⁻² corresponding to TOF of ~ 1 s⁻¹ (Ref ⁹) and for metallic 2D TMDs the
180 values are 0.02 mA-cm⁻² and 0.043 s⁻¹ (Ref ³), suggesting that the turnover for hydrogen
181 evolution is high for 2H phase Nb_{1.35}S₂ catalysts. Summary of the obtained values is provided in
182 Extended Data Table 1.

183

184 Impedance measurements on 2H and 3R Nb_{1.35}S₂ are shown in Figure 3a. It can be seen that the
185 series resistance for the 2H phase Nb_{1.35}S₂ obtained at 1MHz where the phase angle is close to
186 zero is 3.5 Ω due to its high electrical conductivity and indicating good contact with glassy
187 carbon electrode. The charge transfer resistance is 7.4 Ω, facilitating charge injection and
188 transport to active sites. In contrast, the 3R Nb_{1.35}S₂ shows higher resistances and diffusion
189 limited activity. This is in agreement with our observations that the 3R phase is less conducting
190 and is stable at higher film thicknesses. Finally, we have measured the electrochemical stability

191 of the electrodes by carrying out over 10000 cycles. The high current density shows remarkable
192 stability with negligible difference in polarization curves and overpotential values after 10,000
193 cycles (Figure 3b). The above experimental results suggest that intercalation of Nb between 2H
194 phase NbS₂ layers to realize Nb_{1.35}S₂ allow realization of practical current densities of > 5,000
195 mA-cm⁻² – making them potentially useful alternatives to Pt and Ir. To translate the high current
196 densities of 2H phase Nb_{1.35}S₂ catalysts into practical device, we fabricated a proof of concept
197 two electrode electrolyzer for water splitting. The device shown in Figure 3c consists of 2H
198 Nb_{1.35}S₂ on glassy carbon cathode and a commercial Pt anode. The measurements were carried
199 out at room temperature in 0.5 M H₂SO₄. The device characteristics are plotted in Figure 3d,
200 which show that the reaction for the 2H Nb_{1.35}S₂ starts around 1.3 V and the current densities
201 reach 1000 mA-cm⁻² at 2.0 V. Proof of concept electrolyzers of this type typically report current
202 densities of 10 – 100 mA-cm⁻² at similar potential values²⁴.

203

204 To elucidate the fundamental mechanisms responsible for the catalytic performance of 2H
205 Nb_{1.35}S₂, we calculated the thermodynamics of the limiting reaction – the adsorption of hydrogen
206 on the catalyst surface using density functional theory (DFT) including van der Waals
207 interactions. It is well known that the best HER catalysts possess $\Delta G \sim 0$ (that is, thermoneutral
208 condition) so that there is a driving force for hydrogen adsorption on the active site but the
209 binding energy is low to allow efficient hydrogen evolution. The results of the calculations are
210 shown in Figure 4. Our theoretical results suggest that both the Nb and S terminations are stable
211 for the Nb_{1.35}S₂ phases. We have observed intercalated Nb terminated surface by STEM imaging
212 (see Extended Data Fig. 3d). It can be seen in Figure 4a that the free energy for hydrogen
213 adsorption for the 2H Nb_{1.35}S₂ is close to being thermoneutral (~ 0.11 eV) when the surface is
214 terminated by Nb under 0.25 monolayer coverage (Figure 4b). In contrast, the free energy of
215 adsorbed hydrogen is ~ 1 eV when the surface is terminated by sulfur in 2H Nb_{1.35}S₂. The
216 calculations also reveal that the reaction is localized to the surface of the catalysts, as indicated
217 by the charge density diagrams in Figure 4c. The better HER properties of the 2H Nb_{1.35}S₂
218 relative to the 3R Nb_{1.35}S₂ is consistent with the higher density of states at the Fermi level
219 (Figure 4e,f), which translates into higher measured conductivity and better charge transfer
220 kinetics. Thus, our work provides new insight into materials design for achieving high current
221 densities with non-precious metal catalysts.

223 **Figure captions**

224 **Figure 1 | Images of Nb_{1+x}S₂ crystals and atomic structure.** **a**, Atomic force microscopy
225 image of a grown Nb_{1+x}S₂ ($x \sim 0.35$) crystals on high quality glassy carbon (scale bar = 1 μm). **b**,
226 Cross-sectional ADF STEM image of 2H phase Nb_{1.35}S₂ and 3R phase Nb_{1+x}S₂, **c**. The dashed
227 white rectangle represents the unit cell of the structure and the corresponding ball and stick
228 model of the unit cell is shown on the right. The red dashed rectangles in the STEM image and
229 the schematic indicate the positions of the intercalated Nb. Since these sites are partially
230 occupied, the contrast of these planes is lower than of the fully occupied Nb sites. The arrows
231 correlate the locations of the atoms in the STEM image with the atoms in the unit cell. The dark
232 green arrows and spheres in the schematic indicate fully occupied Nb sites and light green
233 arrows and spheres in unit cell indicate partially occupied Nb atoms. Z. A. refers to zone axis of
234 the crystal structure. Scale bar = 5 \AA .

235

236 **Figure 2 | HER catalytic activities of different TMDs.** **a**, Polarization curves for 2H-MoS₂,
237 1T-MoS₂ and WS₂, 2H-Nb_{1.35}S₂, 3R-Nb_{1.35}S₂, 2H-NbS₂ and 3R NbS₂ and Pt measured in 0.5M
238 H₂SO₄ with a scan rate of 5 mVs⁻¹. **b**, Expanded view of the low overpotential region in **a**. The
239 reaction starts immediately upon application of voltage, indicating that the onset potential of 2H-
240 Nb_{1.35}S₂ is < 100 mV and overpotential is 150 mV. **c**, Tafel slopes of different catalysts obtained
241 from polarization curves in **a**. 2H-Nb_{1.35}S₂ shows slope of 43 mV-dec⁻¹ (38 mV-dec⁻¹ after *iR*
242 correction) at low overpotentials (100-130 mV, green) and 70 mV-dec⁻¹ (65 mV-dec⁻¹ after *iR*
243 correction) at high overpotentials (130-200 mV, red). **d**, TOF values of the 2H-Nb_{1.35}S₂ (black
244 line) and other MoS₂-based catalysts reported in the literature^{25,26}. MoS₂ basal planes with sulfur
245 vacancies (blue)²⁷, strained MoS₂ basal planes with sulfur vacancies (green)²⁷ and MoS₂ with
246 low charge transfer resistance, R_c (magenta)¹⁵.

247

248 **Figure 3 | Electrochemical impedance spectroscopy (EIS), electrochemical stability of**
249 **Nb_{1.35}S₂ and proof of concept electrolyzer demonstration.** **a**, Nyquist plots of 2H phase (red
250 curve) and 3R phase Nb_{1.35}S₂. Magnification of 2H-Nb_{1.35}S₂ plot is shown in the inset. The plots
251 (dash line) were fitted using an equivalent circuit to extract the series and charge transfer
252 resistances. **b**, Polarization curves of 2H-Nb_{1.35}S₂ before (black curve) and after (red curve)
253 10,000 cycles. The insets show the percentage of change in overpotential. The error bars are

254 obtained from at least five measurements. **c**, Photograph of the two electrode electrolyzer device
255 consisting of commercial Pt anode and 2H-Nb_{1.35}S₂ cathode. **d**, Polarization curves of water
256 electrolysis showing current density of 1000 mA-cm⁻².

257

258 **Figure 4 | Thermodynamic stability and free-energy calculations for hydrogen evolution for**

259 **2H-Nb_{1.35}S₂ and 3R-Nb_{1.35}S₂ phases.** **a**, The free-energy diagram for hydrogen evolution at
260 standard conditions (1 bar of H₂ and pH=0 at 300 K). The energies of the intermediate states are
261 calculated using BEEF-vdW functional as described in the Methods. A coverage of 0.25 ML was
262 used for all calculations. **b**, Optimized geometries for S- and Nb-terminated surfaces of 2H-
263 Nb_{1.35}S₂ and 3R-Nb_{1.35}S₂ phases. **c**, Charge density difference for H adsorbed on top of Nb-
264 terminated 2H- and 3R-Nb_{1.35}S₂ phases. Most of the charge is localized on the surface, with clear
265 differences between 2H- and 3R-Nb_{1.35}S₂ phases with the former having larger magnitudes. **e-f**,
266 Density of states (DOS) per atom for Nb-terminated 2H- and 3R-Nb_{1.35}S₂ phases projected on
267 different Nb sites. Surface Nb, inner Nb and deep bulk Nb atoms are shown in red, blue and
268 orange, respectively. For a better contrast between the different Nb's atoms, the DOS of surface
269 Nb atoms is highlighted with a filled faint red. Fermi level is set to 0 eV.

270

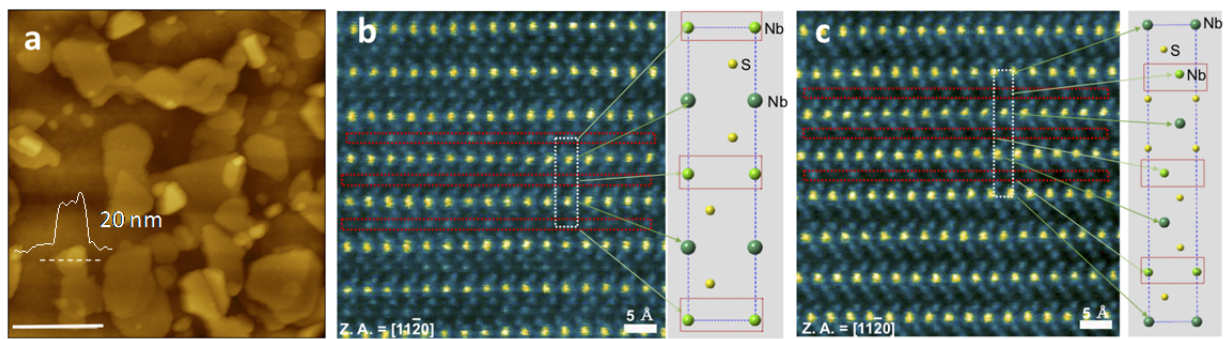
271

272 **Figure 1:**

273

274

275



276

277

278

279

280

281

282

283

284

285

286

287

288

289

290

291

292

293

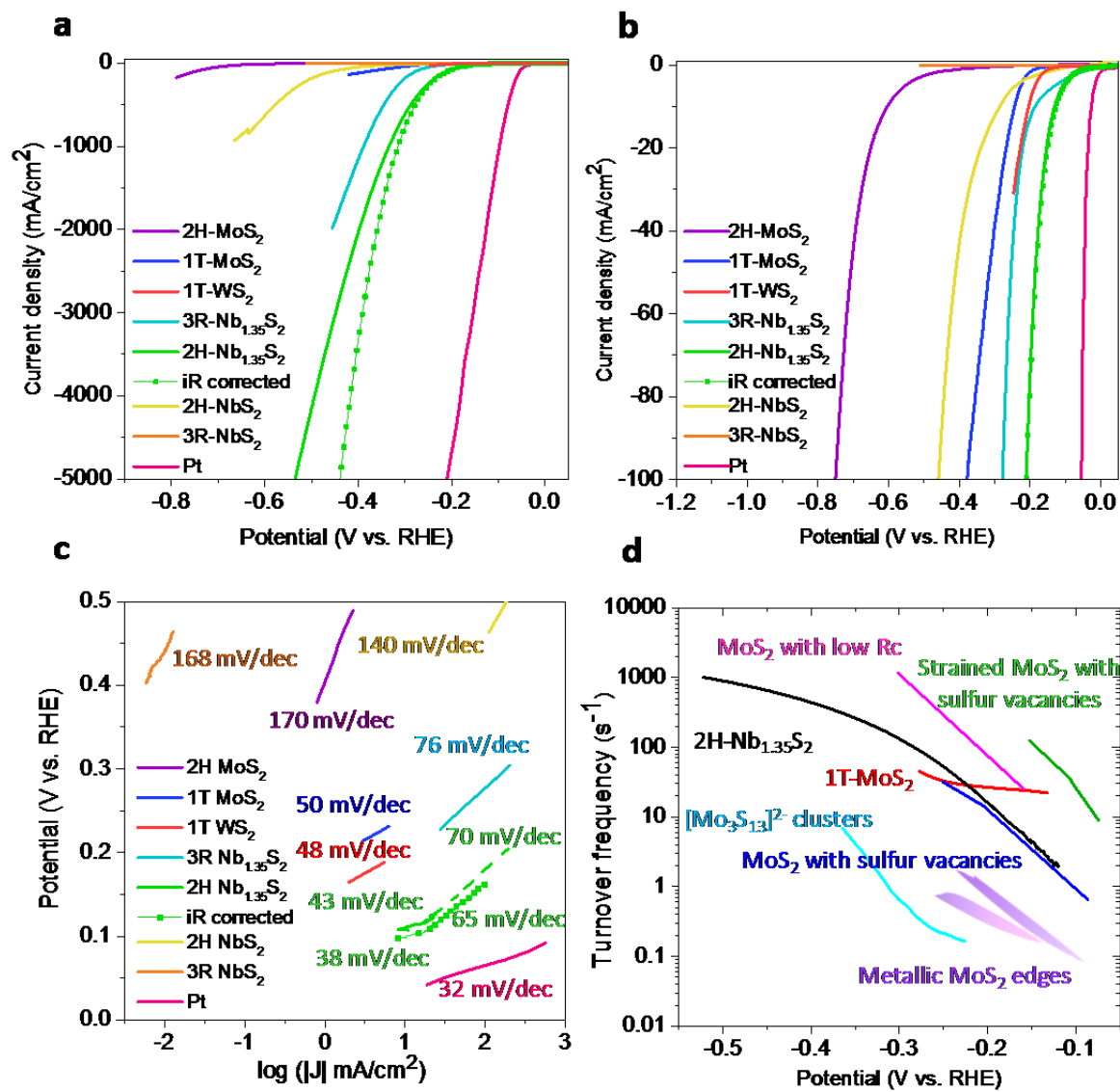
294

295

296

297

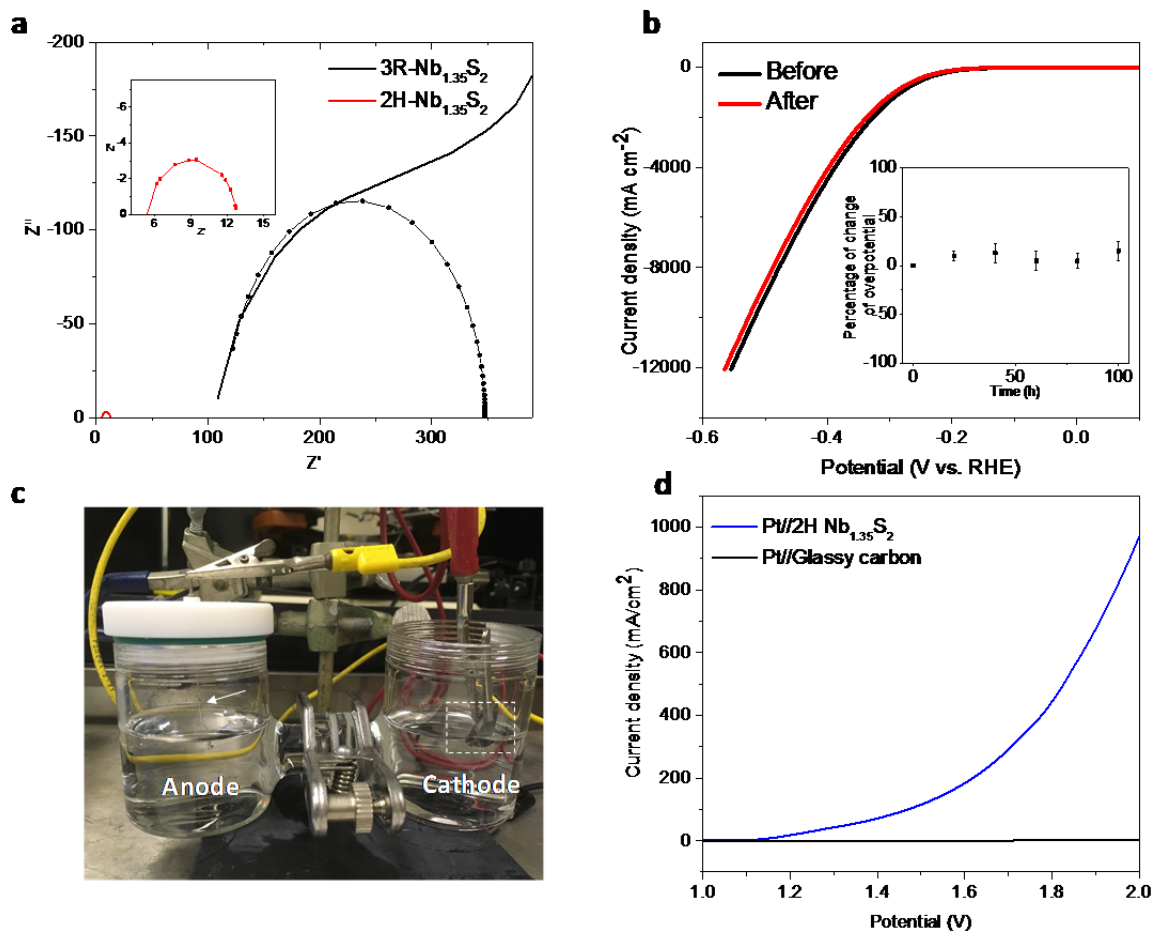
298 **Figure 2**



299

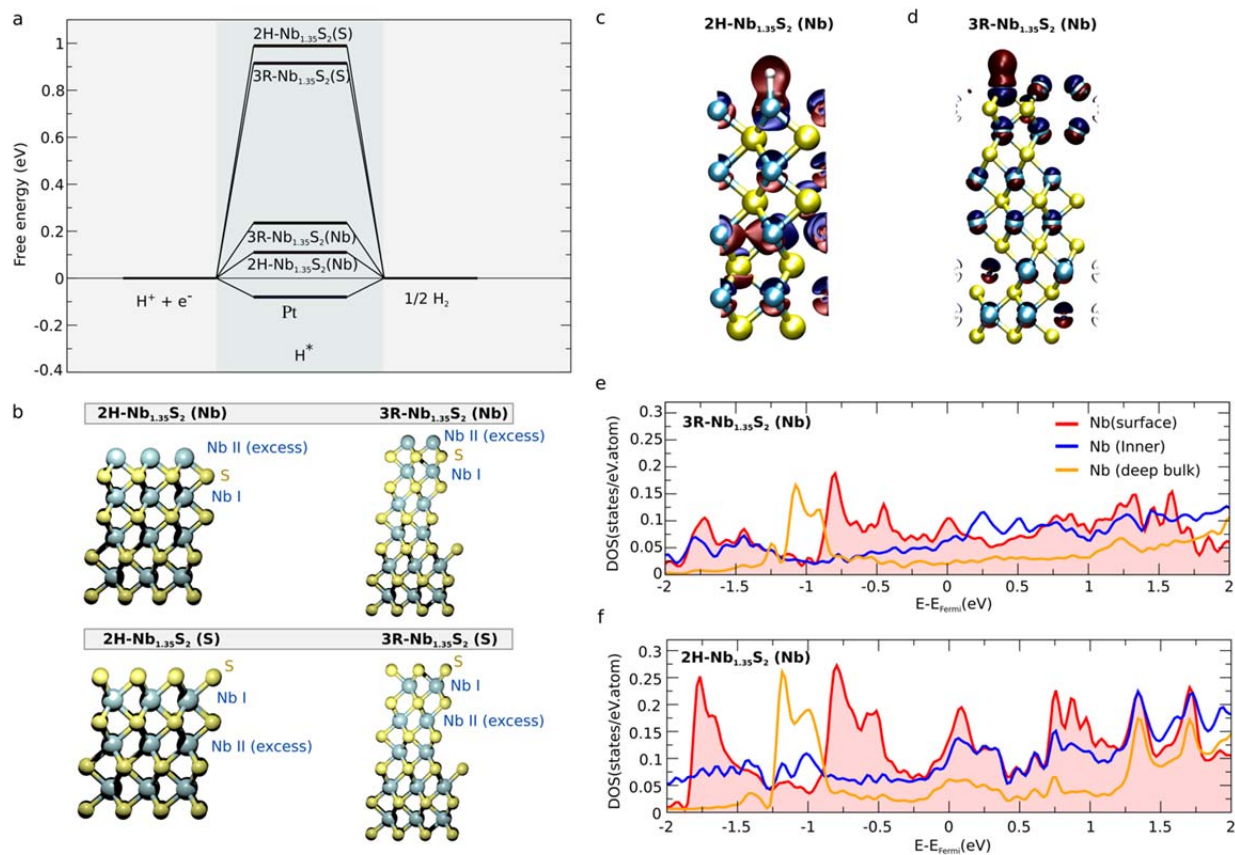
300

301 **Figure 3**
302
303



304

305 **Figure 4**
 306
 307
 308
 309
 310



311
 312
 313
 314
 315
 316
 317
 318
 319
 320
 321
 322
 323
 324
 325
 326
 327

328 **References**

329

330 1. Lukowski, M. A. *et al.* Enhanced Hydrogen Evolution Catalysis from Chemically Exfoliated

331 Metallic MoS₂ Nanosheets. *J. Am. Chem. Soc.* **135**, 10274–10277 (2013).

332 2. Voiry, D. *et al.* Conducting MoS₂ Nanosheets as Catalysts for Hydrogen Evolution Reaction.

333 *Nano Lett.* **13**, 6222–6227 (2013).

334 3. Voiry, D. *et al.* Enhanced catalytic activity in strained chemically exfoliated WS₂ nanosheets

335 for hydrogen evolution. *Nat. Mater.* **12**, 850 (2013).

336 4. Liu, Y. *et al.* Self-optimizing, highly surface-active layered metal dichalcogenide catalysts for

337 hydrogen evolution. *Nat. Energy* **2**, 17127 (2017).

338 5. Shi, J. *et al.* Two-dimensional metallic tantalum disulfide as a hydrogen evolution catalyst.

339 *Nat. Commun.* **8**, 958 (2017).

340 6. Li, H. *et al.* Atomic-Sized Pores Enhanced Electrocatalysis of TaS₂ Nanosheets for Hydrogen

341 Evolution. *Adv. Mater.* **28**, 8945–8949 (2016).

342 7. Yuan, J. *et al.* Facile Synthesis of Single Crystal Vanadium Disulfide Nanosheets by

343 Chemical Vapor Deposition for Efficient Hydrogen Evolution Reaction. *Adv. Mater.* **27**,

344 5605–5609 (2015).

345 8. Chia, X., Ambrosi, A., Lazar, P., Sofer, Z. & Pumera, M. Electrocatalysis of layered Group 5

346 metallic transition metal dichalcogenides (MX₂, M = V, Nb, and Ta; X = S, Se, and Te). *J.*

347 *Mater. Chem. A* **4**, 14241–14253 (2016).

348 9. Jaramillo, T. F. *et al.* Identification of Active Edge Sites for Electrochemical H₂ Evolution

349 from MoS₂ Nanocatalysts. *Science* **317**, 100–102 (2007).

- 350 10. Zhigang, S., Baolian, Y. & Ming, H. Bifunctional electrodes with a thin catalyst layer for
351 'unitized' proton exchange membrane regenerative fuel cell. *J. Power Sources* **79**, 82–85
352 (1999).
- 353 11. Altmann, S., Kaz, T. & Friedrich, K. A. Bifunctional electrodes for unitised regenerative
354 fuel cells. *Electrochimica Acta* **56**, 4287–4293 (2011).
- 355 12. Jellinek, F., Brauer, G. & Müller, H. Molybdenum and Niobium Sulphides. *Nature* **185**,
356 376 (1960).
- 357 13. Merki, D. & Hu, X. Recent developments of molybdenum and tungsten sulfides as
358 hydrogen evolution catalysts. *Energy Environ. Sci.* **4**, 3878–3888 (2011).
- 359 14. Benck, J. D., Hellstern, T. R., Kibsgaard, J., Chakthranont, P. & Jaramillo, T. F.
360 Catalyzing the Hydrogen Evolution Reaction (HER) with Molybdenum Sulfide
361 Nanomaterials. *ACS Catal.* **4**, 3957–3971 (2014).
- 362 15. Voiry, D. *et al.* The role of electronic coupling between substrate and 2D MoS₂
363 nanosheets in electrocatalytic production of hydrogen. *Nat. Mater.* **15**, 1003 (2016).
- 364 16. Yin, Y. *et al.* Contributions of Phase, Sulfur Vacancies, and Edges to the Hydrogen
365 Evolution Reaction Catalytic Activity of Porous Molybdenum Disulfide Nanosheets. *J. Am.*
366 *Chem. Soc.* **138**, 7965–7972 (2016).
- 367 17. Kibsgaard, J., Chen, Z., Reinecke, B. N. & Jaramillo, T. F. Engineering the surface
368 structure of MoS₂ to preferentially expose active edge sites for electrocatalysis. *Nat. Mater.*
369 **11**, 963 (2012).
- 370 18. Kong, D. *et al.* Synthesis of MoS₂ and MoSe₂ Films with Vertically Aligned Layers.
371 *Nano Lett.* **13**, 1341–1347 (2013).

- 372 19. Tsai, C., Abild-Pedersen, F. & Nørskov, J. K. Tuning the MoS₂ Edge-Site Activity for
373 Hydrogen Evolution via Support Interactions. *Nano Lett.* **14**, 1381–1387 (2014).
- 374 20. Eda, G. *et al.* Photoluminescence from Chemically Exfoliated MoS₂. *Nano Lett.* **11**,
375 5111–5116 (2011).
- 376 21. Pan, H. Metal Dichalcogenides Monolayers: Novel Catalysts for Electrochemical
377 Hydrogen Production. *Sci. Rep.* **4**, 5348 (2014).
- 378 22. Tsai, C., Chan, K., Nørskov, J. K. & Abild-Pedersen, F. Theoretical insights into the
379 hydrogen evolution activity of layered transition metal dichalcogenides. *Surf. Sci.* **640**, 133–
380 140 (2015).
- 381 23. Yu, Y. *et al.* Layer-Dependent Electrocatalysis of MoS₂ for Hydrogen Evolution. *Nano*
382 *Lett.* **14**, 553–558 (2014).
- 383 24. Han, N. *et al.* Nitrogen-doped tungsten carbide nanoarray as an efficient bifunctional
384 electrocatalyst for water splitting in acid. *Nat. Commun.* **9**, 924 (2018).
- 385 25. Kibsgaard, J., Jaramillo, T. F. & Besenbacher, F. Building an appropriate active-site
386 motif into a hydrogen-evolution catalyst with thiomolybdate [Mo₃S₁₃]²⁻ clusters. *Nat. Chem.*
387 **6**, 248 (2014).
- 388 26. Xie, J. *et al.* Defect-Rich MoS₂ Ultrathin Nanosheets with Additional Active Edge Sites
389 for Enhanced Electrocatalytic Hydrogen Evolution. *Adv. Mater.* **25**, 5807–5813 (2013).
- 390 27. Li, H. *et al.* Activating and optimizing MoS₂ basal planes for hydrogen evolution through
391 the formation of strained sulphur vacancies. *Nat. Mater.* **15**, 48 (2016).

392
393
394
395
396

397 **Acknowledgments:** MC, JY acknowledge financial support from AFOSR FA9550-16-1-0289.
398 MC, YW acknowledge support from NSF ECCS-1608389. MC and XS acknowledge support
399 from Shenzhen Peacock Plan (Grant No. KQTD2016053112042971). MC and ARM
400 acknowledge financial support from the Ministry of Higher Education Malaysia. HYJ
401 acknowledges the support from Creative Materials Discovery Program through the National
402 Research Foundation of Korea (NRF-2016M3D1A1900035). E.J.G.S. acknowledges the use of
403 computational resources from the UK national high-performance computing service (ARCHER)
404 for which access was obtained via the UKCP consortium (EPSRC grant ref EP/K013564/1); the
405 UK Materials and Molecular Modelling Hub for access to THOMAS supercluster, which is
406 partially funded by EPSRC (EP/P020194/1). The Queen's Fellow Award through the grant
407 number M8407MPH, the Enabling Fund (A5047TSL), and the Department for the Economy
408 (USI 097) are also acknowledged.

409

410 **Author Contributions**

411 MC conceived the idea and supervised the project. JY and ARM designed the experiments with
412 guidance from MC. JY performed the electrochemical measurements and analyses with advice
413 from RF and DV. ARM synthesized the $\text{Nb}_{1.35}\text{S}_2$ samples and characterized them. YW made the
414 devices for HER measurements and made electrical measurements. XS and IB made NbS_2
415 samples and characterized them with the help of FZ. HYJ prepared the FIB samples, performed
416 the STEM analyses on the samples. MA and EJGS provided theoretical insight for the
417 experimental results. MC, HYJ, JY, DV, RF and HS analyzed the data. MC wrote the paper with
418 JY and all of the authors edited the manuscript before submission.

419

420

421

422

423

424

425

426

427

428

429

430

431 **Methods**

432 **Growth of 2H-Nb_{1+x}S₂ and 3R-Nb_{1+x}S₂:** Nb_{1+x}S₂ growth was achieved under low pressure in a
433 horizontal furnace (Lindberg/Blue M) with 1-inch diameter quartz tube. Two small quartz tubes
434 (diameter ~ 9mm) loaded with niobium chloride (NbCl₅, Alfa Aesar, 99.9%) and sulfur powder
435 (Alfa Aesar, 99.5%), were placed upstream of the furnace as shown in Extended Data Fig. 6. The
436 substrates (SiO₂/Si and glassy carbon) were placed face up above an alumina boat in the center
437 zone of the furnace. The tube was initially pumped to a base pressure of 20 Torr for 30min. The
438 furnace was heated up to 850 °C with a ramp rate of 55 °C/min with a flow of 90 sccm Ar. Then,
439 the furnace was heated up to 1000 °C with a ramp rate of 6 °C/min under a flow of 90 sccm
440 H₂/Ar (10% H₂ in Ar). The NbCl₅ was sublimated via a heating belt at 260~300 °C within 5min
441 when the furnace reached to 1000 °C as indicated by the heating cycle shown in Extended Data
442 Fig. 7. After growth for 8 min at 1000 °C, the whole system was naturally cooled down to room
443 temperature.

444
445 **Synthesis of 2H-NbS₂:** 2H-NbS₂ was synthesized by CVD using niobium oxide (Nb₂O₅, 99.9%
446 Sigma-Aldrich) mixed with alkali halide (potassium iodine, KI) and sulfur powder (99.5%, Alfa
447 Aesar). Since niobium oxide has a high melting point, alkali halide is used to create a new
448 eutectic point for the reaction to produce more volatile oxides.²⁸ The mixture of 150 mg of
449 Nb₂O₅ and 100 mg of KI powders in alumina boat was loaded at the center of the tube furnace
450 and SiO₂ substrates were placed above the powder with its polished side facing down. 100 mg of
451 S powder was loaded in the upstream region of the tube. Then, 80 sccm carrier gas (10 % of H₂
452 in Ar) was introduced for 20 min to remove oxygen in the furnace. The furnace was heated with
453 a ramp rate of 33 °C/min to the growth temperatures (1000 °C) and held at 1000 °C for 30 min
454 before cooling down. The upstream region reached 200 °C during the growth. The thin 2H NbS₂
455 crystals and their corresponding Raman spectrum are shown in Extended Data Fig. 8a,b.

456
457 **Synthesis of 3R-NbS₂:** 3R-NbS₂ crystals were grown by a chemical vapor transport (CVT)
458 method which has been employed to prepare other layered compounds.²⁹ Prior to crystal growth,
459 a quartz tube containing high purity source (Nb 99.99% and S 99.99% with a molar ratio of Nb:S
460 is 1:2) was evacuated at 10⁻⁶ Torr and sealed. The sealed quartz tube was then inserted into the
461 tube furnace. The furnace was heated up to 900 °C with a ramp rate of 3°C/min. The reaction

462 time was 18 h at 900 °C and the furnace was cooled down naturally. The CVT grown 3R crystals
463 and the corresponding Raman spectrum are shown in Extended Data Fig. 8c,d.

464
465 **Electrochemical measurements:** Electrochemical measurements were performed in a three-
466 electrode cell using a Versa Stat 3 potentiostat from Princeton Applied research. All
467 measurements were made in 0.5 M H₂SO₄ electrolyte purged with Ar gas. A saturated calomel
468 electrode (Pine Instrument) and glassy carbon were used as the reference electrode and counter
469 electrode, respectively. Extended Data Fig. 9 shows the polarization curves obtained from 2H
470 Nb_{1.35}S₂ using platinum and carbon counter electrode. No noticeable difference was observed,
471 and this excludes any Pt contamination during the measurements. The glassy carbon plate (Ted
472 pella) loaded with 3R- and 2H-Nb_{1.35}S₂ was used as a working electrode. 3R-NbS₂ was dispersed
473 into toluene and sonicated for 1h. The solution was deposited onto glassy carbon electrode (0.1
474 mg/cm²) and dried. 1T-MoS₂ was prepared by the exfoliation of 2H-MoS₂ by n-BuLi following
475 literature.²⁰ 1T-MoS₂ solution was loaded onto glassy carbon electrode (4 μg/cm²) and 2H-MoS₂
476 powder is dispersed into the mixed solution with DI water/IPA (the volume ratio 4:1) and
477 sonicated for 1h to drop onto the glassy carbon electrode. All polarization curves were measured
478 at the scan rate of 5 mVs⁻¹. All potentials are referenced to RHE. In 0.5 M H₂SO₄,
479 E(RHE)=E(SCE) + 0.254 V. Impedance measurements were performed at -0.22 V versus RHE
480 from 1MHz to 0.1 Hz with a 5 mV a.c. amplitude.

481
482 **Device fabrication of 2H-NbS₂:** To demonstrate the HER performance of 2H-NbS₂, we carried
483 out HER test using an electrochemical microcell.¹⁵ We performed e-beam lithography to put gold
484 contacts on as-grown 2H-NbS₂ on SiO₂ (300 nm) substrate. The gold electrodes were deposited
485 via e-beam evaporation under high vacuum conditions (10⁻⁷ Torr). After this process, we
486 performed another e-beam lithography step to open a window on 2H-NbS₂ and cover the gold
487 electrodes to avoid contact with electrolyte. The device is shown in Extended Data Fig. 10.
488 Electrochemical measurements were performed in 0.5 M H₂SO₄ and glassy carbon and Ag/AgCl
489 electrodes were used as counter and reference electrodes, respectively.

490
491

492 **Electrochemical surface area measurements:** The estimation of electrochemically active
 493 surface area was conducted by measurement of the double-layer capacitance in a potential region
 494 with no faradaic response. Cyclic voltammetric (CV) measurements were performed between
 495 285 mV and 315 mV vs. RHE at various scan rates from 5 mVs⁻¹ to 100 mVs⁻¹ in order to
 496 estimate the double layer capacitance (C_{dl}), see Extended Data Fig. 5. Roughness factor (RF) was
 497 estimated from the ratio of the measured double layer capacitance with respect to the specific
 498 capacitance of glassy carbon electrode (0.87 mF/cm²). Our image analysis of the electrode
 499 surface (Extended Data Fig. 4) shows that only ~ 20% of the glassy carbon electrode is covered
 500 by the catalyst. Therefore, to calculate the RF, we take the areal capacitance of the glassy carbon
 501 after catalyst deposition to be (0.87 mF-cm⁻²)(0.8) = 0.7 mF-cm⁻². Thus, the RF is given by:

$$RF = \frac{9.6 \text{ mF cm}^{-2}}{0.7 \text{ mF cm}^{-2}} = 13.7$$

504 **Turnover frequency calculation:** According to previous literature, turnover frequency can be
 505 obtained following equation.

$$TOF (s^{-1}) = \frac{J \left(\frac{A}{cm^2} \right)}{n \times N \times RF \times (1.602 \times 10^{-19} C)}$$

506 To determine the density of active sites (N), we assume the lattice constant of 2H-Nb_{1.35}S₂ is 3.31
 507 Å (Figure 1c, STEM image). n is the number of electrons involved in the reaction. The surface
 508 area of unit cell can be $9.4 \times 10^{-16} \text{ cm}^2$. We assumed that entire basal plane can be catalytically
 509 active. Therefore, the density of active is estimated to be about $1.06 \times 10^{15} \text{ cm}^{-2}$. The density of
 510 the surface active sites of 2H Nb_{1.35}S₂ on geometric area : $1.06 \times 10^{15} \text{ sites/cm}^2 \times 13.7 = 1.4 \times$
 511 $10^{16} \text{ sites/cm}^2$

512 To get TOF at exchange current density, the exchange current density was extrapolated linearly
 513 from the Tafel slope. The exchange current density of 2H-Nb_{1.35}S₂ is 800 μA/cm² which is
 514 remarkable value among the reported TMD based catalysts as listed in Extended Data Table 1.

515
 516 **Electrical conductivity measurements:** The conductivity of the intercalated phases was
 517 measured and by evaporating gold contacts and is shown in Extended Data Fig. 11. We find the
 518 2H Nb_{1.35}S₂ phase to be highly conducting compared to other reports in the literature.³⁰⁻³³

519

520 **Computational Methods:** The calculations were done using the plane wave density functional
521 theory (DFT) Vienna ab-initio simulation package (VASP)³⁴⁻³⁷ The van der Waals interactions
522 were taken into account at the level of opt-B88 functional³⁸ and the Bayesian error estimation
523 exchange-correlation functional with long-range interactions³⁹ (BEEF-vdW). A 500 eV plane-
524 wave cutoff was used, and the Brillouin zone was sampled with a Monkhorst-Pack⁴⁰ sampling of
525 3x3x1 k-points grid for the relaxation and a 15x15x1 k-points for the energy calculations. The
526 ΔG_H were calculated using the formula:

$$\Delta G_H = \Delta E + \Delta(ZPE) - T\Delta S$$

528
529 with
530

$$\Delta E = E(\text{surface} + H) - E(\text{surface}) - \frac{1}{2}E(H_2)$$

531

$$\Delta(ZPE) = ZPE_H - \frac{1}{2}ZPE_{H_2}$$

532

$$T\Delta S = \frac{-1}{2}TS_{H_2} = -0.205eV$$

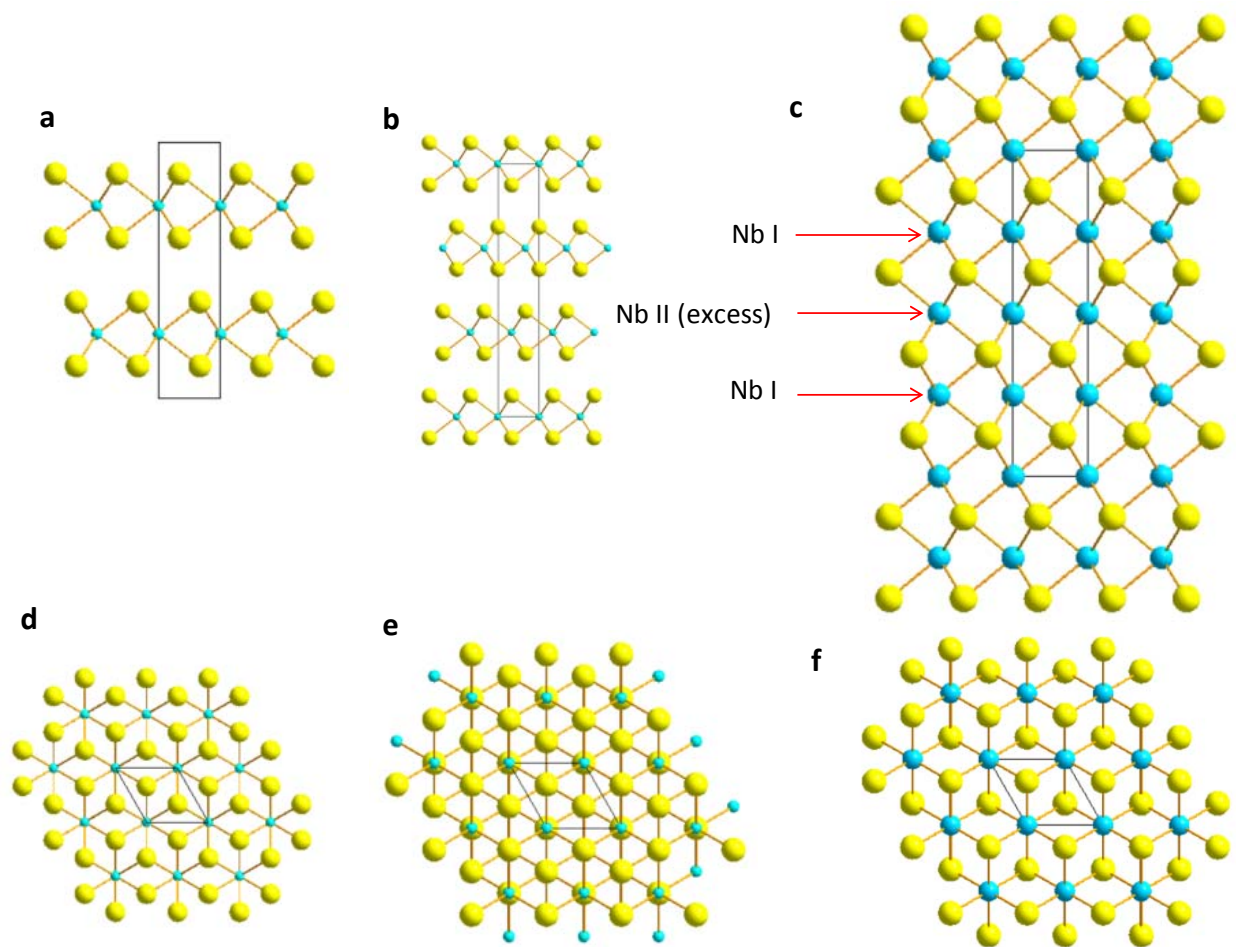
533

534

535 Where $E(\text{surface} + H)$ is the total energy of the system with the H-atom bound at the basal
536 plane, $E(\text{surface})$ is the total energy of the pristine system, $E(H_2)$ is the total energy of the H_2
537 molecule. $\Delta(ZPE)$ is the difference between the zero-point energy (ZPE) of the H-atom and the
538 zero-point energy of the H_2 molecule, calculated using the normal mode analysis. We will use
539 the entropy of the molecular hydrogen in the gas phase at standard conditions (1 bar of H_2 , pH=0
540 and T=300 K).

541 The bulk lattice parameters calculated using ab initio opt B88-vdW and BEEF-vdW functionals
542 are shown in Extended Data Tables 3 and 5, as well their energetics as displayed in Extended
543 Tables 4, 6, 7 and 8. The corresponding crystal structures obtained from these parameters are
544 shown in Extended Data Figure 12.

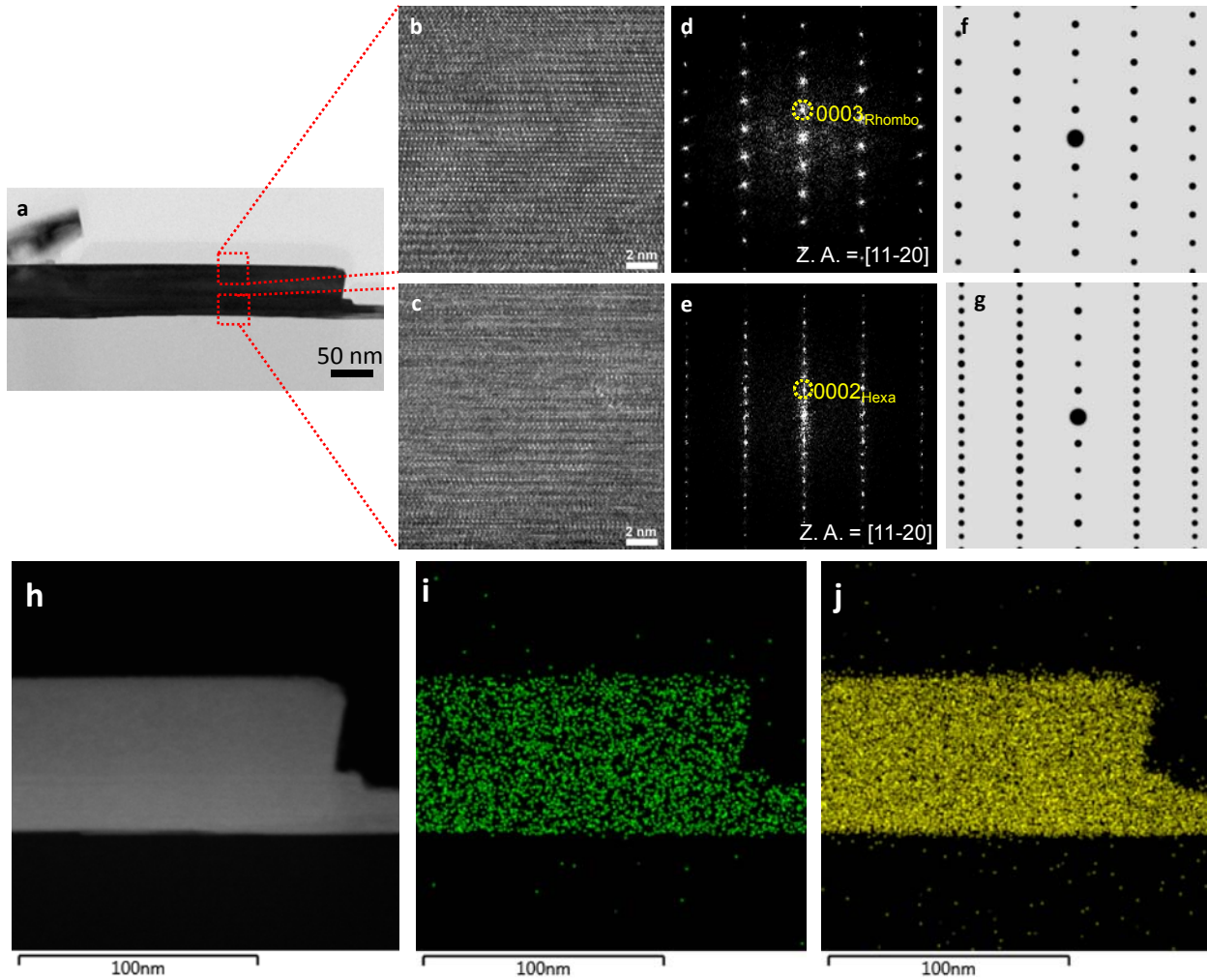
545
546
547
548



549
550 **Extended Data Fig. 1 | Phases of NbS₂.** (a, b) Side view and (d, e) top view of 2H hexagonal
551 (P63/mmc symmetry) and 3R rhombohedral (R3m symmetry) phases of NbS₂. (c, f) Side and top
552 views of 2H phase Nb_{1.35}S₂ phase. The excess of Nb (labelled as Nb II in the c) occupies
553 octahedral configuration while the Nb I are in trigonal prismatic sites. The Nb_{1.35}S₂ phase can
554 also occur in the 3R phase.

555
556
557
558

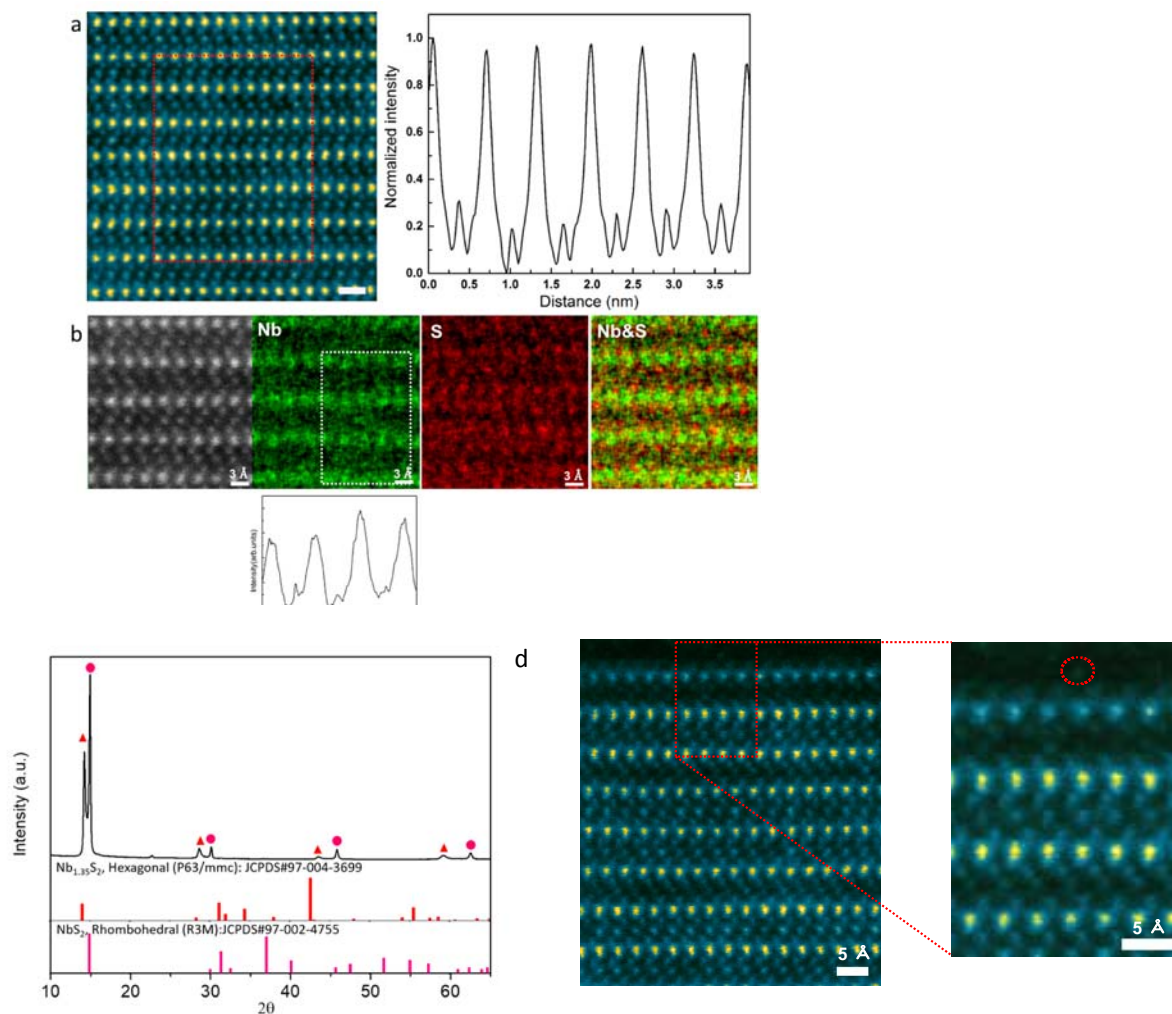
559
560



561

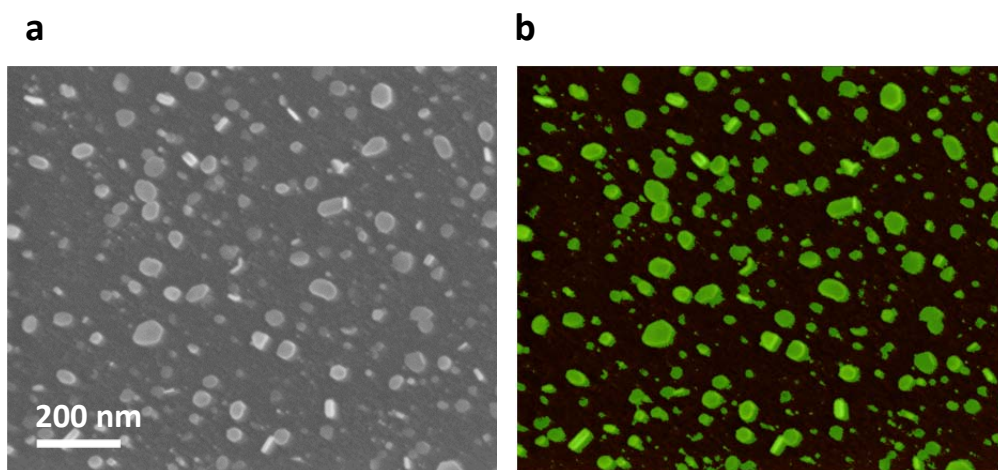
562

563 **Extended Data Fig. 2 | TEM of $\text{Nb}_{1.35}\text{S}_2$ and corresponding diffraction images.** **a**, Low
564 magnification BFTEM image of cross-sectional FIB sample (thickness = 40 nm) prepared from
565 CVD grown samples on SiO_2 . **b**, **c** HRTEM images taken from top of the sample and bottom of
566 the sample as indicated by square dotted regions on the left image. **d**, **e** Fast Fourier transform
567 (FFT) pattern indicating that the top (thicker) region is rhombohedral while the bottom (thin)
568 region is in hexagonal configuration based on their very good agreement with simulated patterns
569 shown in **f** (simulated ED patterns for intercalated 3R phase) and **g** (simulated ED for
570 intercalated 2H phase). **h**, Low magnification of image of the FIB cross section and the
571 corresponding Energy Dispersive Spectroscopy map showing Nb (**i**) and S (**j**) in the sample.

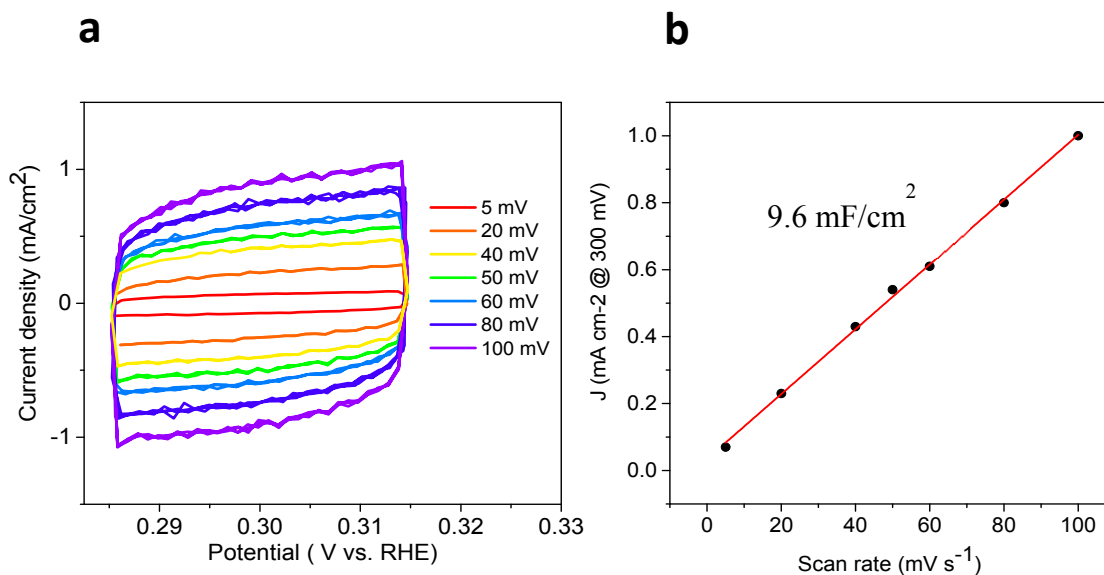


572
 573 **Extended Data Fig. 3 | Line scan and chemical analyses in STEM.** **a**, Annular dark field
 574 image (left) and the corresponding (right) intensity line scan of 2H Nb_{1.35}S₂ phase showing that
 575 Nb atoms are present between the layers. **Scale bar = 5 Å.** **b**, Black and white unfiltered STEM
 576 image and corresponding elemental maps of Nb, S, and both Nb and S obtained using energy
 577 dispersive x-ray spectroscopy. The mapping and the line scan below the Nb map confirm that the
 578 intercalated atoms are Nb. **c**, X-ray diffraction of Nb_{1.35}S₂. The spectrum matches JCPDS#97-
 579 004-3699 for hexagonal phase Nb_{1.35}S₂, indicated by the triangles. In particular, the presence of
 580 additional diffraction peak at ~14.3° indicates excess Nb. The structure is a combination of
 581 layered NbS₂ and intercalated 2H Nb_{1.35}S₂ – completely consistent with our STEM results. **d**,
 582 STEM image of 2H phase Nb_{1.35}S₂ with an enlargement of the surface region shown on the right.
 583 Faint images of Nb atoms terminating the surface can be observed as indicated by the dotted red
 584 circle.

585
586
587
588
589
590
591
592
593
594
595
596
597
598
599

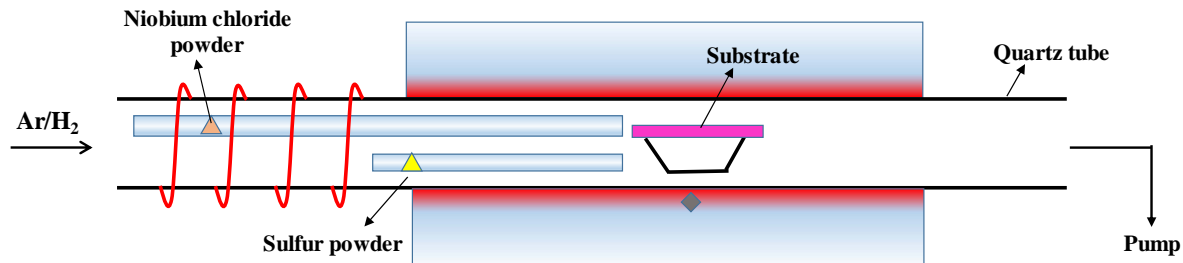


600 **Extended Data Fig. 4 | Image analyses of areal coverage of catalysts on electrode surface. a,**
601 SEM image of 2H-Nb_{1.35}S₂. **b,** Image analyses was used to highlight (in green) the Nb_{1.35}S₂
602 flakes on the glassy carbon electrode (black background). Then the percent of area covered by
603 the flakes was calculated. A total of 15 images were taken and the average area covered by the
604 catalyst Nb_{1.35}S₂ flakes was approximately 20 % ± 3% of the electrode surface.



605

606 **Extended Data Fig. 5 | Electrochemical surface area measurements. a,** CV curves of Nb_{1.35}S₂
607 electrodes measured between 285 and 315 mV vs. RHE. **b,** Current density at 300 mV plotted
608 against cyclic voltammetry scan rate.
609
610



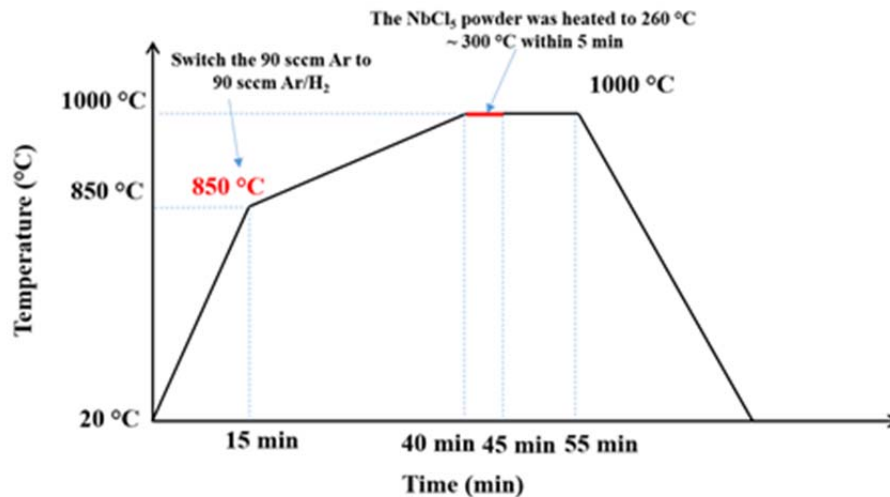
611

612 **Extended Data Fig. 6 | Schematic of chemical vapor deposition setup for Nb_{1+x}S₂ synthesis.**

613 The precursors are placed upstream because they sublime at a much lower temperature than the
614 growth temperature.

615

616



617

618 **Extended Data Fig. 7 | Heating ramp and cooling cycle growth of Nb_{1+x}S₂.** The tube furnace

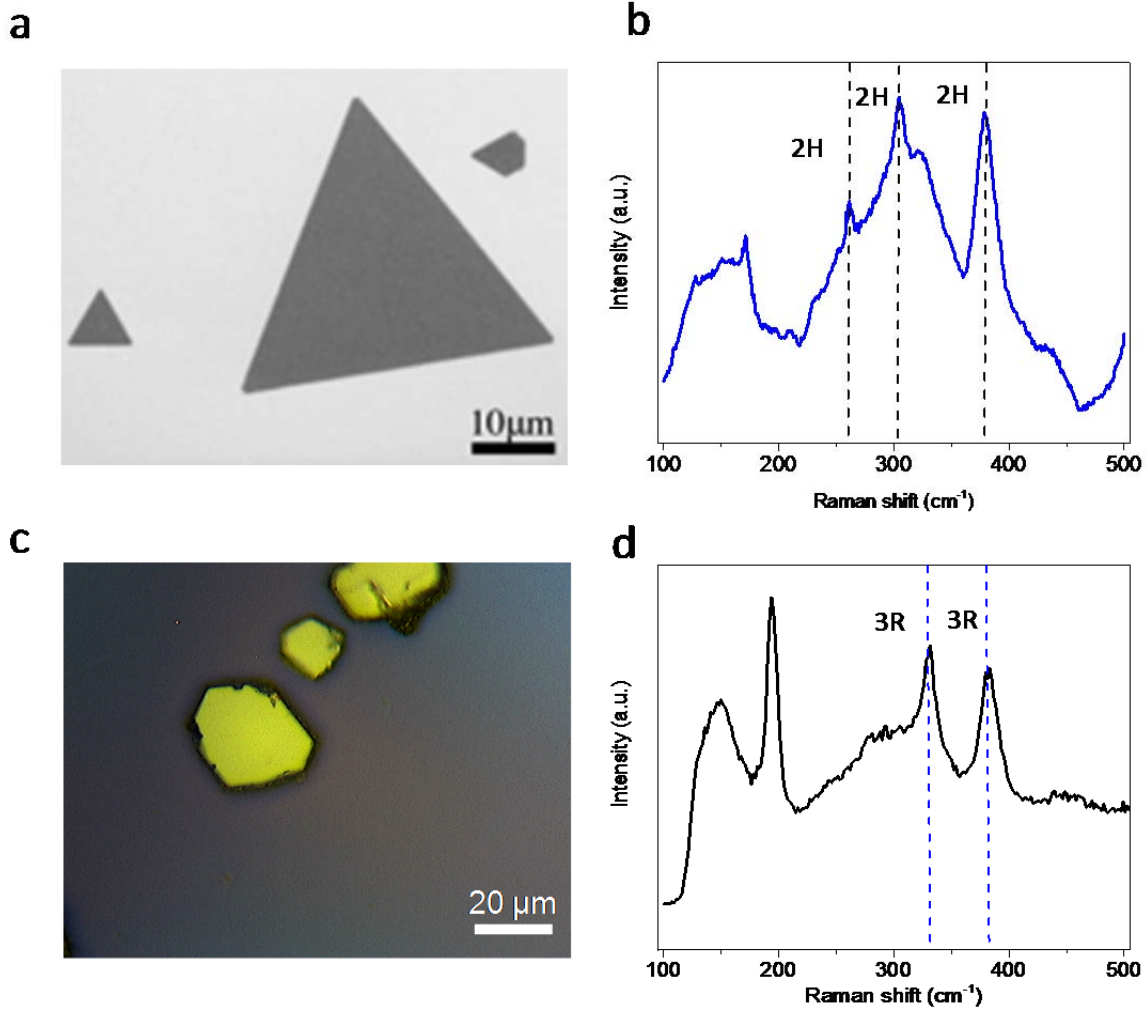
619 was initially heated in Ar atmosphere, then in reducing atmosphere and growth was conducted
620 for 10 – 20 minutes to achieve different thicknesses.

621

622

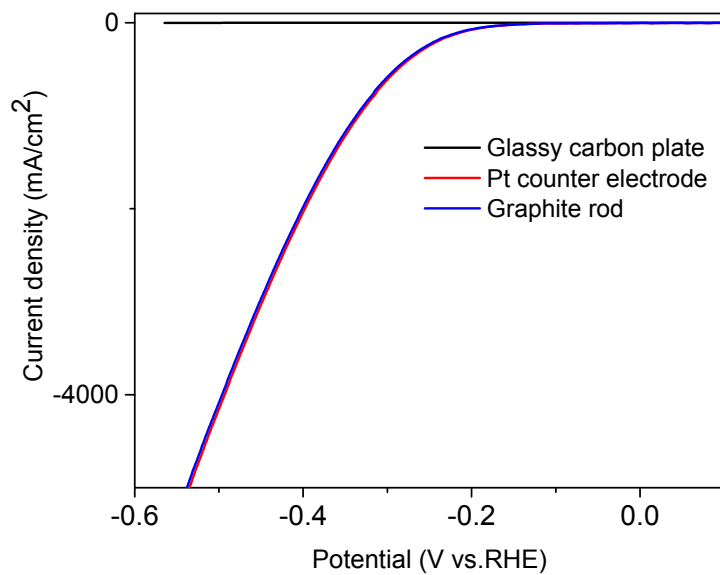
623

624



625
 626 **Extended Data Fig. 8 | Different phases of NbS₂.** **a**, SEM image of CVD grown 2H-NbS₂ with
 627 lateral dimensions of 5-20 μm and **b**, Raman spectrum of 2H-NbS₂ shows E_{1g}, E¹_{1g}, A_{1g} at 260,
 628 304 and 379 cm⁻¹ respectively. **c**, Optical microscope image of 3R-NbS₂ grown by CVT and **d**,
 629 Raman spectrum of 3R-NbS₂ shows E_{2g} and A_{1g} peaks at 330 cm⁻¹ and 385 cm⁻¹, respectively.

630
 631
 632
 633
 634
 635
 636



637

638 **Extended data Fig. 9** | Pt vs glassy carbon as counter electrode. Polarization curves for glassy
639 carbon plate and 2H Nb_{1.35}S₂ using Pt or carbon as counter electrode.

640

641

642

643

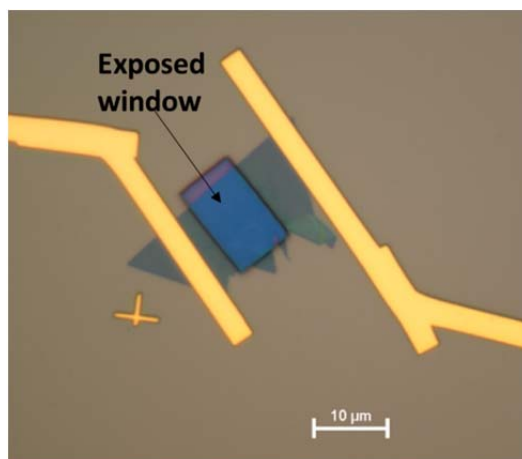
644

645

646

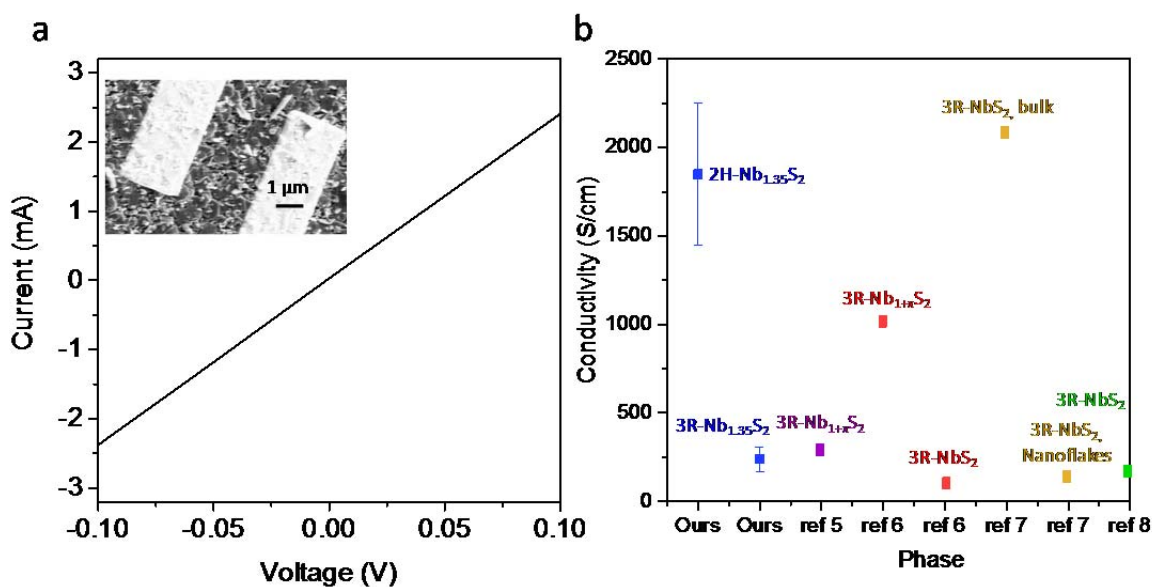
647

648



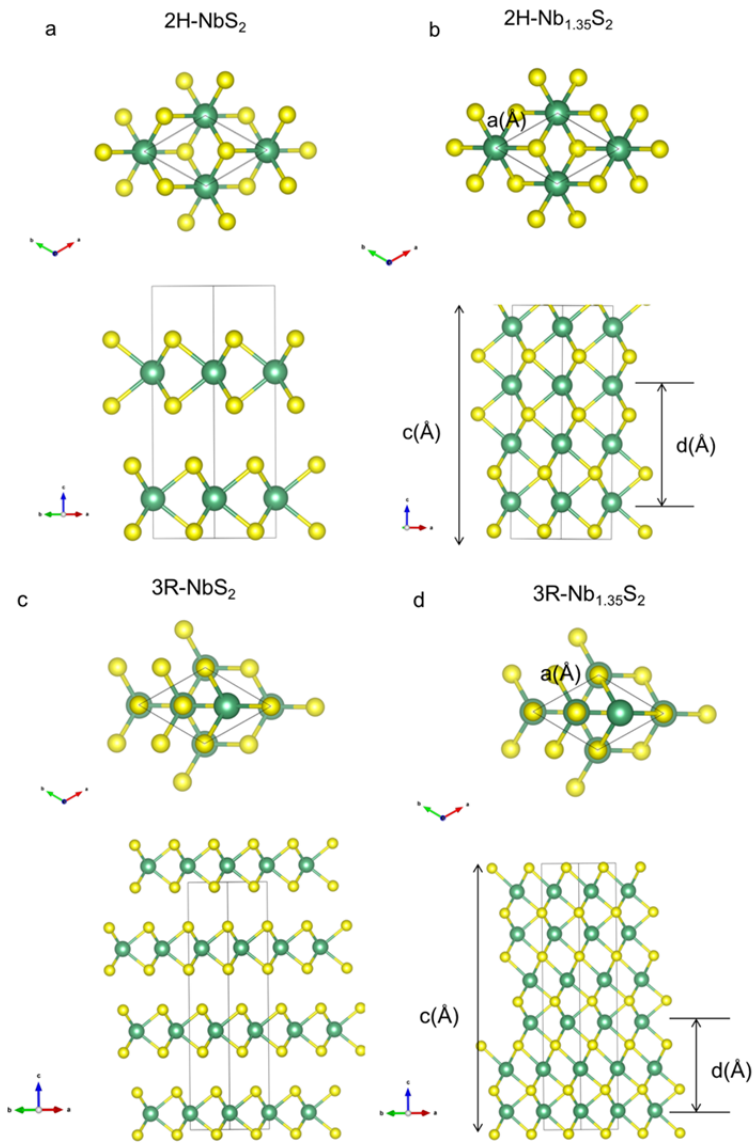
649
650

651 **Extended data Fig. 10 | Electrochemical microcell devices.** Optical image of an
652 electrochemical microcell with 2H-NbS₂ as the catalyst. The blue region is the NbS₂ flake and
653 rectangular gold contacts are patterned onto it. A window is opened lithographically so that
654 catalysis measurements can be made. The entire area is covered by PMMA except the window so
655 the electrolyte can only interact with the catalyst.



656
657
658
659
660
661
662
663

Extended data Fig. 11 | Electrical properties of different NbS₂. **a**, I-V curve measured for the
2H Nb_{1.35}S₂ nanoflakes. The inset shows a SEM image of the device. An average value of 1800
S/cm was obtained with the highest value being > 2400 S/cm. **b**, Comparison of conductivities
for NbS₂. NbS₂ is known as a metallic TMD material. However, the conductivity values in
literature are scattered.^{30–33}



664

665

666

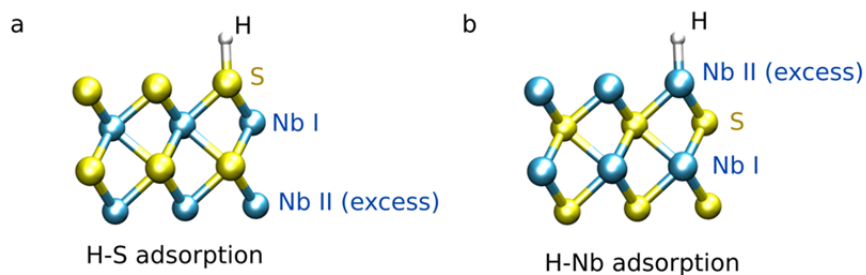
667

668 **Extended data Fig. 12** | Definition of geometrical parameters used at Extended Data Table 3 at

669 regular 2H-NbS_2 and 3R-NbS_2 phases as well as in the intercalated $2\text{H-Nb}_{1.35}\text{S}_2$, $3\text{R-Nb}_{1.35}\text{S}_2$

670 phases.

671



672
673

674 **Extended data Fig. 13** | Definition of the geometry utilized to calculate the energetics of H at a
675 monolayer NbS₂ with an additional Nb layer into the system. This would correspond to the
676 smallest “intercalated phase” before it established in a 2H or 3R phases. The energetics for these
677 systems are shown in Extended Data Table 7.

678

679

680 **Extended Data Table 1** | Comparison of TOF and exchange current density of TMDs catalysts

	J_0 ($\mu\text{A}/\text{cm}^2$)	TOF at J_0	<i>ref</i>
2H-Nb _{1.35} S ₂	800 ± 100	0.17s ⁻¹ ± 0.03	Our work
2H-MoS ₂ /Au	7.9	-	9
1T-WS ₂	20	0.043	3
2H-TaS ₂	100-179.47	-	5
Pt	450	0.9	9

681

682

683

Extended Data Table 2 | Parameters used for synthesis of Nb_{1+x}S₂

	NbCl ₅	S	Temperature of NbCl ₅
3R-Nb _{1+x} S ₂	35 mg	200 mg	300 °C
2H-Nb _{1+x} S ₂	20 mg	100 mg	260 °C

684

685

686

687

688

689

690

691

692

693

694 **Extended Data Table 3 | Bulk lattice parameters using opt-B88 functional.** Simulations of
 695 the geometrical parameters using opt-B88 functional including vdW interactions. Lattice
 696 parameter, $a(\text{\AA})$, interlayer distance via Nb-Nb distance, $d(\text{\AA})$, and supercell length, $c(\text{\AA})$ are
 697 defined as in Extended Data Figure 12. Sound comparison with experimental data at different
 698 phases is observed.

	2H-NbS ₂		3R-NbS ₂		2H-Nb _{1.35} S ₂		3R-Nb _{1.35} S ₂
	Theory	Exp.	Theory	Exp.	Theory	Exp.	Theory
$a(\square)$	3.34	3.31	3.35	3.33	3.31	3.306	3.24
$d(\square)$	5.97	5.91	6.05	5.98	6.64	6.35	6.81
$c(\square)$	11.935	11.89	18.17	17.81	13.29	12.6	20.43

699
 700
 701 **Extended Data Table 4 | Thermodynamic properties of S terminated surface using opt-B88**
 702 **functional.** Energetics of the intercalated phase 2H-Nb_{1.35}S₂ with adsorption of H at S atoms at
 703 different coverages using opt-B88 functional. The large values of ΔG_H (eV) at different
 704 coverages rule out any HER using S-terminate surfaces.

Coverage	2H-Nb _{1.35} S ₂ (H-S adsorption)		
	0.11 ML	0.25 ML	1 ML
ΔE (eV)	1.011	0.804	1.459
ZPE (eV)	0.203	0.203	0.162
ΔG_H (eV)	1.245	1.077	1.694

705
 706 **Extended Data Table 5 | Bulk lattice parameters using BEEF-vdW functional.** Simulations
 707 of the geometrical parameters using BEEF-vdW functional including vdW interactions. Lattice
 708 parameter, $a(\text{\AA})$, interlayer distance via Nb-Nb distance, $d(\text{\AA})$, and supercell length, $c(\text{\AA})$ are
 709 defined as in Extended Data Figure 12. Sound comparison with experimental data at different
 710 phases is obtained.

	2H-NbS ₂		3R-NbS ₂		2H-Nb _{1.35} S ₂		3R-Nb _{1.35} S ₂
	Theory	Exp.	Theory	Exp.	Theory	Exp	Theory
$a(\square)$	3.35	3.31	3.35	3.33	3.30	3.30	3.22
$d(\square)$	6.34	5.91	6.36	5.98	6.65	6.35	6.65
$c(\square)$	12.67	11.89	19.10	17.81	13.30	12.6	19.94

712
 713 **Extended Data Table 6 | Thermodynamic properties of S terminated surface using BEEF-**
 714 **vdW functional.** Energetics of the intercalated phases $2\text{H-Nb}_{1.35}\text{S}_2$ and $3\text{R-Nb}_{1.35}\text{S}_2$ with
 715 adsorption of H at S atoms at different coverages using BEEF-vdW functional. Similarly as in
 716 the opt-B88 functional, the S-terminated surface seems inert for HER as long as H atoms bind on
 717 S.

	2H-Nb _{1.35} S ₂ (H-S adsorption)			3R-Nb _{1.35} S ₂ (H-S adsorption)
Coverage	0.11 ML	0.25 ML	1 ML	0.25 ML
ΔE (eV)	1.005	0.766	1.41	0.619
ZPE (eV)	0.226	0.226	0.16	0.226
ΔG_{H} (eV)	1.302	0.989	1.64	0.915

718
 719
 720 **Extended Data Table 7 | Thermodynamic properties of a monolayer NbS₂ with additional**
 721 **Nb atoms in the structure.** Energetics of the monolayer NbS₂ with additional Nb atoms
 722 incorporated into the structure (see Extended Data Fig. 13). This system corresponds to the
 723 smallest situation where the effect of additional Nb atoms could be appreciated on the free
 724 energies and HER of monolayer NbS₂. The adsorption of H is simulated either at S-terminated
 725 the surface or at Nb-terminated. The large variations in energy between both configurations
 726 indicate the H adatoms would prefer binding at the Nb sites rather than on S. This suggests that
 727 additional Nb atoms have a strong effect on the chemical kinetics of the reaction changing the
 728 preferable site of H adsorption for efficient HER. Similar results as those in Ref. 22 are
 729 compared for the monolayer NbS₂ without additional Nb atoms. Calculations at the level of
 730 BEEF-vdW functional.

	Monolayer NbS ₂	Monolayer NbS ₂ Nb terminated (H-S adsorption)	Monolayer NbS ₂ Nb terminated (H-Nb adsorption)
Coverage	0.0625 ML	0.25 ML	0.25 ML
ΔE (eV)	-0.185	1.039	0.072
ZPE (eV)	0.226	0.215	0.098
ΔG_{H} (eV)	0.11	1.324	0.24

731

732
733
734
735
736
737
738

Extended Data Table 8 | Thermodynamic properties of Nb terminated slab with adsorption of H on Nb atoms. Energetics of the intercalated phases 2H-Nb_{1.35}S₂ and 3R-Nb_{1.35}S₂ with adsorption of H on Nb atoms using BEEF-vdW functional. The resulting geometries are those shown in Figure 4. The comparison between 2H-Nb_{1.35}S₂ and 3R-Nb_{1.35}S₂ clearly indicates that the former would give better HER results than the latter, as it follows closely the measurements.

	2H-Nb _{1.35} S ₂ (Nb Terminated)	3R-Nb _{1.35} S ₂ (Nb Terminated)
Coverage	0.25 ML	0.25 ML
ΔE (eV)	-0.056	0.066
ZPE (eV)	0.099	0.098
ΔG_H (eV)	0.11	0.235

739
740
741

- 742 28. Li, S. *et al.* Halide-assisted atmospheric pressure growth of large WSe₂ and WS₂
743 monolayer crystals. *Appl. Mater. Today* **1**, 60–66 (2015).
- 744 29. Suh, J. *et al.* Doping against the Native Propensity of MoS₂: Degenerate Hole Doping by
745 Cation Substitution. *Nano Lett.* **14**, 6976–6982 (2014).
- 746 30. Huang, Y. H., Peng, C. C., Chen, R. S., Huang, Y. S. & Ho, C. H. Transport properties in
747 semiconducting NbS₂ nanoflakes. *Appl. Phys. Lett.* **105**, 93106 (2014).
- 748 31. Molenda, J., Bak, T. & Marzec, J. Electrical and electrochemical properties of niobium
749 disulphide. *Phys. Status Solidi A* **156**, 159–168 (1996).
- 750 32. Niazi, A. & Rastogi, A. K. Low-temperature resistance minimum in non-superconducting
751 3R-Nb_{1+x}S₂ and 3R-Ga_xNbS₂. *J. Phys. Condens. Matter* **13**, 6787 (2001).
- 752 33. Zhao, S. *et al.* Two-dimensional metallic NbS₂: growth, optical identification and
753 transport properties. *2D Mater.* **3**, 25027 (2016).

- 754 34. Kresse, G. & Hafner, J. Ab initio molecular dynamics for liquid metals. *Phys. Rev. B* **47**,
755 558–561 (1993).
- 756 35. Kresse, G. & Hafner, J. Ab initio molecular-dynamics simulation of the liquid-
757 metal\char21 {}amorphous-semiconductor transition in germanium. *Phys. Rev. B* **49**, 14251–
758 14269 (1994).
- 759 36. Kresse, G. & Furthmüller, J. Efficiency of ab-initio total energy calculations for metals
760 and semiconductors using a plane-wave basis set. *Comput. Mater. Sci.* **6**, 15–50 (1996).
- 761 37. Kresse, G. & Furthmüller, J. Efficient iterative schemes for ab initio total-energy
762 calculations using a plane-wave basis set. *Phys. Rev. B* **54**, 11169–11186 (1996).
- 763 38. Klimeš, J., Bowler, D. R. & Michaelides, A. Chemical accuracy for the van der Waals
764 density functional. *J. Phys. Condens. Matter* **22**, 22201 (2010).
- 765 39. Wellendorff, J. *et al.* Density functionals for surface science: Exchange-correlation model
766 development with Bayesian error estimation. *Phys. Rev. B* **85**, 235149 (2012).
- 767 40. Monkhorst, H. J. & Pack, J. D. Special points for Brillouin-zone integrations. *Phys. Rev.*
768 *B* **13**, 5188–5192 (1976).
- 769
- 770
- 771